Modeling of Globulitic Alloy Solidification with Convection

J. NI and C. BECKERMANN[1]
Department of Mechanical Engineering
The University of Iowa
Iowa City, IA 52242, USA

Abstract: A numerical study of solidification of a metal alloy with a globulitic morphology is reported. The model is based on a previously developed two-phase approach that incorporates descriptions of the heat transfer, solute redistribution, melt convection, and solid transport on the system scale with microscopic models of nucleation, thermal and solutal undercoolings, grain growth and impingement. Results obtained for solidification of an Al-4%Cu alloy in a rectangular cavity cooled from a side reveal extensive macrosegregation and nonuniformities in the grain size distribution due to the motion of the solid and liquid phases. The presence of considerable uncertainties in the modeling of nucleation and interfacial transport phenomena is emphasized.

INTRODUCTION

THE compositional and structural characteristics of a solidified metal alloy are determined, to a large extent, by the mass, momentum, heat and species transport phenomena that occur during the solidification process. An important consideration in the modeling of solidification is the coupling of the transport phenomena occurring on the system (or macroscopic) scale with the formation and growth of the crystals on a microscopic scale. Microstructures present during solidification of metal alloys can be divided into two groups, namely (1) columnar structures that consist of long, aligned dendrite arms that are attached to the mold wall, such that the heat is removed through the solid in a direction opposite to the growth direction, and (2) equiaxed or globulitic structures consisting of crystals that grow radially into an undercooled melt. Whereas thermal and solutal convection of the melt and the resulting macrosegregation during columnar solidification have received considerable research attention in recent years (Incropera and Viskanta, 1990), the study of transport phenomena during globulitic solidification has been neglected. Important additional issues that need to be addressed in the modeling of globulitic solidification are the origin and nucleation of the solid grains, their unconstrained growth and impingement, and their movement in the (convecting) melt. For example, the transport and sedimentation of small crystals is fundamental to the development and extent of the globulitic zone and the bottom cone of negative segregation observed in castings (Flemings, 1974).

Considerable progress in the modeling of equiaxed or globulitic metal alloy solidification has been made through the use of a so-called micro-macroscopic approach that couples macroscopic heat flow calculations with microscopic models of nucleation, grain growth, and impingement (Thevoz et al., 1989; Rappaz, 1989; Stefanescu et al., 1990). However, these studies have neglected melt convection and solid transport. The present paper describes a first attempt at modeling globulitic alloy solidification in the presence of gravity-induced liquid and solid convection. The model is based on the recently developed two-phase approach for alloy solidification (Ni and Beckermann, 1990, 1991). In this approach, the coupling between microscopic and macroscopic phenomena is achieved through (1) volume averaging of the microscopic

[1]Author to whom correspondence should be addressed.
Paper received January 10, 1993.

1062-0656/93/02 0217-15 $6.00/0

NOMENCLATURE

a	exponent in Table 4
A	area (m²)
c	specific heat (J/kg³-K)
C	concentration of a chemical species, i.e., mass fraction
C_{de}	generalized drag coefficient
C_{ie}	generalized inertial coefficient
C_{ke}	generalized Kozeny coefficient
d_s	mean particle diameter (m)
$\mathbf{D}$	coefficient of diffusion tensor (m²/s)
E	exponent in Table 4
$\mathbf{g}$	gravitational acceleration vector (m/s²)
h	average convective heat transfer coefficient (W/m²-K)
h_k	specific enthalpy of phase k (J/kg)
h_m	average convective mass transfer coefficient (m/s)
$\mathbf{j}$	species flux (kg/m²-s)
K_1, K_2	coefficients in Equation (3)
$\mathbf{k}$	thermal conductivity tensor (W/m-K)
L	latent heat of fusion (J/kg)
l	diffusion length (m)
$\mathbf{M}$	interfacial momentum transfer rate per unit volume (N/m³)
n	grain density (1/m³)
$\dot{n}$	generation rate of crystals (1/m³-s)
p	pressure (N/m²)
Pr	Prandtl number
$\mathbf{q}$	heat flux (W/m²)
R	grain radius (m)
Re	multiphase Reynolds number
Sc	Schmidt number
S_v	interfacial area concentration (1/m)
t	time(s)
T	temperature (K)
$\mathbf{v}$	velocity (m/s)
V	volume (m³)

Greek Symbols

Γ	interfacial mass transfer rate due to phase change (kg/m³-s)
δ	correction factor (see Table 4)
ϵ_k	volume fraction of phase k
κ	segregation coefficient
μ	dynamic viscosity (Ns/m²)
ϱ	density (kg/m³)
χ_k	phase function
Ψ_k	a quantity of phase k

Subscripts

d	drag
e	eutectic
f	final
k	phase k
i	interfacial
in	initial
l	liquid phase
m	melting
nu	nucleation
s	solid phase or single
sp	solid packing
o	averaging volume

Superscripts

d	dissipative
j	solute transfer rate
q	heat transfer rate
$-$	interfacial average
$*$	effective or macroscopic

transport equations and (2) the use of separate conservation equations for the liquid and solid phases together with interfacial balances. This study extends previous calculations by Prakash (1990a, 1990b), who utilized a highly simplified version of a two-phase model. In a similar manner as in the micro-macroscopic models (Rappaz, 1989), the present model includes nucleation, thermal and solutal undercoolings at the growth front, and grain impingement. However, this exploratory study is limited to a simple binary alloy (Al-4%Cu) solidifying with a globulitic morphology in which the free grains are assumed to be spherical. The results illustrate the effects of melt convection and grain movement on macrosegregation and the final grain size distribution.

MODEL EQUATIONS

The system considered is illustrated in Figure 1 and consists of a rectangular cavity contain-

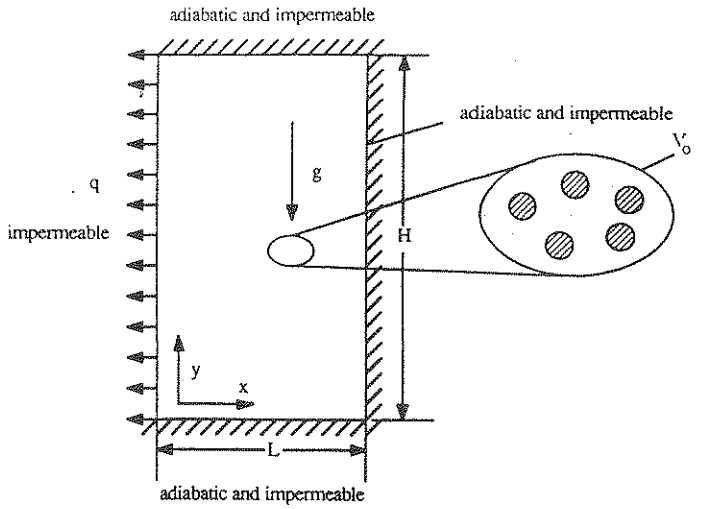

Figure 1. *Illustration of the physical system.*

ing an Al-4%Cu alloy. The walls are impermeable and adiabatic, except for the left vertical wall at which a constant heat flux, q, is applied. The alloy is initially in the liquid state and quiescent at a uniform temperature and concentration, T_{in} and C_{in}, respectively. The volume averaged mass, momentum, energy and species conservation equations for each phase ($k = l,s$), together with the corresponding interfacial balances, are taken directly from Ni and Beckermann (1990, 1991) and are shown in Table 1. All dispersive fluxes are neglected. In these equations, the intrinsic volume average and the interfacial average of a quantity, Ψ_k, are defined, respectively, as

$$\langle \Psi_k \rangle^k = \frac{1}{V_k} \int_{V_o} X_k \Psi_k dV; \qquad \overline{\Psi}_{ki} = \frac{1}{A_i} \int_{A_i} \Psi_k dV \tag{1}$$

All symbols are defined in the Nomenclature. The boundary conditions for the momentum equations are zero-velocity conditions for the liquid velocity and the normal component of the solid velocity, and slip conditions for the tangential solid velocity component (Ding and Gidaspow, 1990). The macroscopic or effective thermal conductivities, mass diffusivities, and liquid viscosity are assumed equal to their microscopic counterparts. The expression for the effective solid viscosity shown in Table 1 is an approximation that is based on available models for Newtonian flow of solid/liquid mixtures (Ni, 1991). The term ϵ_{sp} is the maximum solid packing fraction above which the grains merge and cannot move. Other details can be found in Ni and Beckermann (1991). Note that the phase change rate, Γ_s, is calculated from the interfacial energy and species balances as a function of the thermal, $\overline{T}_{ki} - \langle T_k \rangle^k$, and solutal, $\overline{C}_{ki} - \langle C_k \rangle^k$, undercoolings. Expressions relating the various interfacial quantities and the enthalpy and density to temperature and concentration are provided in Table 2. The phase diagram is assumed to be linear and the enthalpy is assumed to be a function of temperature only, with a constant specific heat. Thus, the latent heat of fusion is given by: $\overline{h}_{li} - \overline{h}_{si} = (c_l - c_s)T_i + L$. The densities are assumed constant, except for the liquid density in the buoyancy term in the liquid momentum equation (see Table 2). Because $\varrho_l = \varrho_l(T_l, C_l)$ and $\varrho_l \neq \varrho_s$ in the buoyancy terms, the model accounts for thermosolutal natural convection in the melt as well as floating/sedimentation of solid crystals. More accurate property relations could be incorporated into the model. All thermophysical properties and other system parameters are summarized in Table 3.

The remaining quantities that need to be modeled can be found in the interfacial balances and are, therefore, part of the microscopic modeling effort. The expressions used are summarized in Table 4. Before impingement ($\epsilon_s < \epsilon_{sp}$), the interfacial area concentration, $S_v = A_i/V_o$, is given by the exact expression for spheres because of the assumed spherical

TABLE 1. Macroscopic Conservation Equations and Interfacial Balances (k = s, l, and $\epsilon_s + \epsilon_l = 1$).

Mass: $$\frac{\partial}{\partial t}(\epsilon_k \rho_k) + \nabla \cdot (\epsilon_k \rho_k \langle \mathbf{v}_k \rangle^k) = \Gamma_k$$

Interfacial mass balance: $$\Gamma_s + \Gamma_l = 0$$

Momentum: $$\frac{\partial}{\partial t}(\epsilon_k \rho_k \langle \mathbf{v}_k \rangle^k) + \nabla \cdot (\epsilon_k \rho_k \langle \mathbf{v}_k \rangle^k \langle \mathbf{v}_k \rangle^k) = -\epsilon_k \nabla \langle p_k \rangle^k + \bar{\mathbf{v}}_{ki} \Gamma_k + \mathbf{M}_k^d + \epsilon_k \rho_k \mathbf{g}$$

$$+ \nabla \cdot \{\mu_k^* [\nabla(\epsilon_k \langle \mathbf{v}_k \rangle^k) + [\nabla(\epsilon_k \langle \mathbf{v}_k \rangle^k)]^t - \langle \mathbf{v}_s \rangle^s \nabla \epsilon_k - \nabla \epsilon_k \langle \mathbf{v}_s \rangle^s]\}$$

$$\langle p_l \rangle^l = \langle p_s \rangle^s$$

Interfacial momentum balance: $$\mathbf{M}_s^d = -\mathbf{M}_l^d = \frac{3}{4} \frac{\epsilon_s}{d_s} \rho_l C_{de} |\langle \mathbf{v}_l \rangle^l - \langle \mathbf{v}_s \rangle^s| (\langle \mathbf{v}_l \rangle^l - \langle \mathbf{v}_s \rangle^s)$$

Energy: $$\frac{\partial}{\partial t}(\epsilon_k \rho_k \langle h_k \rangle^k) + \nabla \cdot (\epsilon_k \rho_k \langle \mathbf{v}_k \rangle^k \langle h_k \rangle^k) = \nabla \cdot (\mathbf{k}_k^* \cdot \epsilon_k \nabla \langle T_k \rangle^k) + \bar{h}_{ki} \Gamma_k + \frac{S_v k_k}{l_k^q} (\bar{T}_{ki} - \langle T_k \rangle^k)$$

Interfacial energy balance: $$(\bar{h}_{li} - \bar{h}_{si}) \Gamma_s = \left[\frac{S_v k_l}{l_l^q} (\bar{T}_{li} - \langle T_l \rangle^l) + \frac{S_v k_s}{l_s^q} (\bar{T}_{si} - \langle T_s \rangle^s) \right]$$

Species: $$\frac{\partial}{\partial t}(\epsilon_k \rho_k \langle C_k \rangle^k) + \nabla \cdot (\epsilon_k \rho_k \langle \mathbf{v}_k \rangle^k \langle C_k \rangle^k) = \nabla \cdot (\mathbf{D}_k^* \cdot \rho_k \epsilon_k \nabla \langle C_k \rangle^k) + \bar{C}_{ki} \Gamma_k$$

$$+ \frac{S_v \rho_k D_k}{l_k^i} (\bar{C}_{ki} - \langle C_k \rangle^k)$$

Interfacial species balance: $$(\bar{C}_{li} - \bar{C}_{si}) \Gamma_s = \left[\frac{S_v \rho_l D_l}{l_l^i} [\bar{C}_{li} - \langle C_l \rangle^l) + \frac{S_v \rho_s D_s}{l_s^i} (\bar{C}_{si} - \langle C_s \rangle^s) \right]$$

Effective transport properties: $\mu_l^* = \mu_l$; $\mu_s^* = \dfrac{[1 - \epsilon_s/\epsilon_{sp}]^{-2.5\epsilon_{sp}} - \epsilon_l}{\epsilon_s} \mu_l$; $\mathbf{k}_k^* = k_k$; $\mathbf{D}_k^* = D_k$

TABLE 2. Property Relations.

Enthalpy relations:

$$\bar{h}_{li} = c_l \bar{T}_{li} + L; \quad \bar{h}_{si} = c_s \bar{T}_{si}; \quad \langle h_l \rangle^l = c_l \langle T_l \rangle^l + L$$

$$\langle h_s \rangle^s = c_s \langle T_s \rangle^s; \quad \bar{T}_{li} = \bar{T}_{si} = T_i$$

Liquid density relation (Ganesan and Poirier, 1987) for buoyancy term:

$$1/\rho_l = [0.397 - 0.4522 \langle C_l \rangle^l + 4.0924 \times 10^{-5} (\langle T_l \rangle^l - 273.15)$$

$$+ 1.1078 \times 10^{-4} \langle C_l \rangle^l (\langle T_l \rangle^l - 273.15) + 0.27475 \langle C_l \rangle^{l2}] \times 10^{-3}$$

Equilibrium phase diagram relations:

Primary solidification: $$\bar{C}_{li} = \frac{C_e (T_m - T_i)}{T_m - T_e}; \quad \bar{C}_{si} = \varkappa \bar{C}_{li}$$

Eutectic solidification: $$T_i = T_e; \quad \bar{C}_{li} = C_e; \quad \bar{C}_{si} = C_e$$

*TABLE 3. Thermophysical Properties and System Data.**

Properties (unit)	Numerical Value
Cavity dimensions H & L (m × m)	0.1 × 0.05
Initial and boundary data	
Initial temperature of the liquid phase, T_{in} (K)	930.0
Initial concentration of the liquid phase, C_{in} (weight fraction)	0.04
Constant heat flux at the left wall, q (W/m²)	-10^6
Property data	
Density of the liquid phase, ϱ_l (kg/m³) (except in buoyancy term)	2450.0
Density of the solid phase, ϱ_s (kg/m³)	2450.0
Dynamic viscosity of the liquid phase, μ_l (N-s/m²)	0.0012
Maximum solid packing fraction, ϵ_{sp}	0.637
Thermal conductivity of the liquid phase, k_l (W/m-K)	77.0
Thermal conductivity of the solid phase, k_s (W/m-K)	153.0
Specific heat of the liquid phase, c_l (J/kg-K)	1179.0
Specific heat of the solid phase, c_s (J/kg-K)	766.0
Latent heat of fusion, L (J/kg) (for $c_l = c_s$)	397 × 10^3
Mass diffusivity of the liquid phase, D_l (m²/s)	5.0 × 10^{-9}
Mass diffusivity of the solid phase, D_s (m²/s)	8.0 × 10^{-3}
K_1 (1/m³-s)	10^{11}
K_2 (s/m³K²)	0
Segregation coefficient, $\varkappa$	0.173
Eutectic temperature, T_e (K)	821.2
Eutectic concentration, C_e (weight fraction)	0.327
Melting temperature of "solvent," T_m (K)	933.5
Initial grain diameter, d_{si} (m)	10^{-6}

*Thermophysical properties are taken from Battle and Pehlke (1990) and Hatch (1984).

growth morphology. For $\epsilon_s > \epsilon_{sp}$, the factor $\delta(\epsilon_s)$ accounts for the reduction in the interfacial area due to merging of the solid/liquid interfaces within the averaging volume (Ni et al., 1990). Similarly, the assumed spherical geometry allows for a simple calculation of the local grain radius from the knowledge of the solid fraction and the number of grains per unit volume. The grain density, n, is calculated from the following conservation equation (Ni and Beckermann, 1990, 1991):

$$\frac{\partial n}{\partial t} + \nabla \cdot (\langle \mathbf{v}_s \rangle^s n) = \dot{n} \tag{2}$$

The term $\dot{n}$ is the nucleation rate. The nucleation rate is calculated from the instantaneous nucleation model of Stefanescu et al. (1990), i.e.,

$$\dot{n} = K_1 + K_2 \left(\frac{dT}{dt} \right)^2 \tag{3}$$

For simplicity, K_2 is taken to be zero (see Table 3), nucleation is assumed to occur at the liquidus temperature, and the initial grain diameter, d_{si}, is taken as 10^{-6} m. If grains are advected into regions of higher temperature and remelt to a diameter below d_{si}, the local value of the grain density is reset to zero. The validity of the above nucleation model in the presence of solid and liquid convection has not been established. Other nucleation models could be utilized instead.

The drag coefficient, C_{de}, is calculated from a generalized expression derived by Agarwal and O'Neill (1988) that is valid for all solid fractions (see Table 4). In the limit of $\epsilon_s \to 0$, C_{de} reduces to the drag coefficient for a single sphere (e.g., Stokes' law for $Re \to 0$). For $\epsilon_s > 0.5$, the grains form a packed bed and the expression for C_{de} together with the interfacial momentum balance (see Table 1) reduces to Ergun's equation, and the Kozeny-Carman expression for the permeability of packed beds can be recovered (Ni, 1991).

TABLE 4. Geometric and Interfacial Relations.

Interfacial area concentration (Ni et al., 1990): $S_v = (36\pi n)^{1/3}\epsilon_s^{2/3}\delta(\epsilon_s)$

where $\delta(\epsilon_s) = 1 \quad \epsilon_s \le \epsilon_{sp}; \quad \delta(\epsilon_s) = \left(\frac{\epsilon_s}{\epsilon_{sp}}\right)^{1/3}\left(\frac{1-\epsilon_s}{1-\epsilon_{sp}}\right)^{1-\epsilon_{sp}\,1/3\,\epsilon_{sp}} \quad \epsilon_s > \epsilon_{sp}$

Mean radius of the solid grains: $R_s = d_s/2 = \left[\frac{3\epsilon_s}{4\pi n}\right]^{1/3}$ Final grain radius: $R_f = \left[\frac{3}{4\pi n}\right]^{1/3}$

Drag coefficient (Agarwal and O'Neill, 1988; Ni, 1991):

$$C_{de} = \left\{\frac{24 \times 2C_{ke}(1-\epsilon_l)}{Re} + C_{ie}\right\}; \quad Re = \frac{\varrho_l \epsilon_l |\langle \mathbf{v}_l\rangle^l - \langle \mathbf{v}_s\rangle^s| d_s}{\mu_l}$$

$C_{ke} = 25/6; \qquad C_{ie} = 7/3 \qquad \epsilon_l \le 0.5$

$$C_{ke} = \frac{1}{2}\frac{\epsilon_l^3}{1-\epsilon_l}\left[\frac{1 + 4.7(1-\epsilon_l)}{1 - 1.83(1-\epsilon_l)}\right]; \quad C_{ie} = \frac{24(10^E - 1)}{Re[1 - 0.9(\epsilon_l - 0.25)^{1/3}(1-\epsilon_l)^{2/3}]^3}; \quad \epsilon_l > 0.5$$

$$E = 0.261Re^{0.369} - 0.105Re^{0.431} - \frac{0.124}{1 + (\log_{10}Re)^2}$$

Diffusion lengths (Rowe and Claxton, 1965; Ni, 1991):

$$l_l^q(\text{or } l_l^t) = \left[\frac{1}{\frac{1}{1-\epsilon_s^{1/3}} + \frac{1}{3\epsilon_l}Pr^{1/3}(\text{or } Sc^{1/3})Re^a}\right]R_s; \quad a = \frac{2Re^{0.28} + 4.65}{3(Re^{0.28} + 4.65)}$$

$$l_s^q(\text{or } l_s^t) = \frac{R_s}{5}$$

The meanings of the interfacial heat and species diffusion lengths, l_k^q and l_k^t, are illustrated in Figure 2. In the presence of convection, the liquid diffusion lengths can be identified with convective heat and mass transfer coefficients through $h = k_l/l_l^q$ and $h_m = D_l/l_l^t$, respectively. The correlation by Rowe and Claxton (1965) is utilized for the liquid diffusion lengths because it includes proper dependencies on the solid fraction and reduces to the single sphere limit for $\epsilon_s \to 0$. In the absence of convection (i.e., $Re = 0$), the correlation reduces to l_l^q or $l_l^t = (1 - \epsilon_s^{1/3})R_s$, which roughly approximates the solution of the (steady) spherical diffusion equation in the liquid space around each grain (i.e., $R_f - R_s$). The expression for the solid diffusion length (see Table 4) is based on parabolic temperature and species profiles in the spherical grain. The validity of the expressions for the diffusion lengths for the present system are not known, and they should only be viewed as first approximations. During the eutectic reaction, the interfacial species balance (see Table 1) is meaningless and the liquid and solid species diffusion lengths are set to an arbitrarily large number. During remelting, the solid interfacial species concentration is set equal to the volume-averaged species concentration of the solid phase.

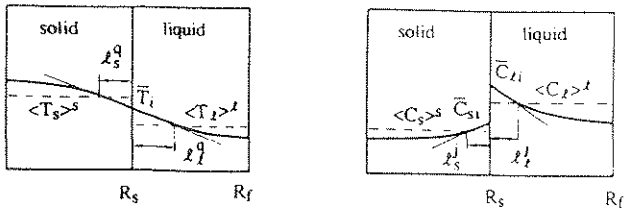

Figure 2. *Illustration of heat and species diffusion lengths.*

NUMERICAL PROCEDURES

The model equations were solved using the PHOENICS computer code, which is one of the few commercially available codes with a built-in two-phase capability. All constitutive, property, and interfacial relations can be programmed in user-accessible subroutines. The conservation equation for the grain density [Equation (2)] was discretized separately using the upwind scheme in a manner consistent with the discretization scheme employed in PHOENICS for the other conservation equations. Other details can be found in the *PHOENICS User Manual* (Ludwig et al., 1989).

Special procedures were developed for the calculation of the four dependent variables: Γ_s (or Γ_l), T_i, C_{li}, and C_{si}. They appear in the interfacial energy and species balances and the phase diagram relations in a complicated and implicit fashion. In addition, different procedures are required for primary ($T_i > T_e$) and eutectic ($T_i = T_e$) solidification, as well as for remelting. For example, for primary solidification, the interfacial energy and species balances are combined to derive two quadratic equations for T_i and Γ_s (Ni, 1991). On the other hand, during eutectic solidification, the interfacial species balance is meaningless (because $C_{li} = C_{si} = C_e$) and the phase change rate, Γ_s, is calculated from the sum of the solid and liquid energy conservation equations (with $T_i = T_e$). The same is done during remelting, except that during "primary remelting" (with $T_i > T_e$) the interfacial liquid concentration, C_{li}, is obtained from the interfacial species balance (with $C_{si} = \langle C_s \rangle^s$), and the interfacial temperature, T_i, is obtained from the liquidus line of the phase diagram (see Tables 1 and 2). These and other procedures proved to be critical for achieving fast and stable convergence during each time step. For conciseness, they will be detailed in a separate publication.

The calculations were performed on an IBM 3090 computer. A grid system of 25 × 25 nodal points was utilized for the calculations presented in this paper. The grid was slightly skewed towards the domain boundaries. Although this grid system may not be sufficient to produce grid independent results, it represents a reasonable compromise between accuracy and computational time. The time step was reduced until time step independent results were obtained. The numerical code was carefully checked and validated for several limiting cases, such as solidification without liquid convection and solid transport, and sedimentation of spheres without solidification (Ni, 1991; Feller, 1991; Feller and Beckermann, 1993).

RESULTS AND DISCUSSION

In order to illustrate several model features, a preliminary simulation was performed where liquid convection and solid transport were deactivated and the domain was reduced to a single control volume. Figure 3 shows the calculated cooling curve (i.e., temperature versus time). Due to the high value of the thermal diffusivity relative to the mass diffusivity, the solid and liquid phases are nearly in thermal equilibrium so that only one (mixture) temperature is shown.

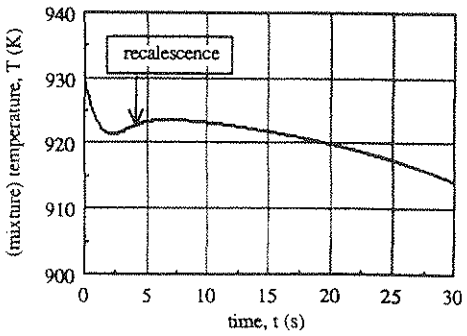

Figure 3. *Cooling curve showing the recalescence phenomenon predicted by the two-phase model.*

Solidification is controlled by solutal undercooling, i.e., by the microscopic species concentration gradients on each side of the solid/liquid interface. The cooling curve shows the recalescence phenomenon and can only be predicted if nucleation and undercooling are considered (Thevoz et al., 1989). The temperature increase during the recalescence period is due to the fact that the latent heat release rate is larger than the external cooling rate. After nucleation, the solute rejected from the solid builds up in the liquid in front of the solid/liquid interfaces within the control volume, causing a large degree of solutal undercooling and, hence, a large solidification rate. Later, diffusion results in a more uniform liquid concentration on the microscopic scale and reduced solutal undercooling. A more thorough investigation of globulitic solidification in such a zero-dimensional geometry using the present two-phase model can be found elsewhere (Feller, 1991; Feller and Beckermann, 1993).

Results of the two-dimensional simulation including liquid convection and solid transport are illustrated in Figures 4 to 7, corresponding to 10 s, 30 s, 60 s, and 90 s. Solidification is complete at 117 s, and the final patterns are displayed in Figure 8. All conditions are as specified in Table 4. Figure 4(a) shows the liquid velocity vectors, $\langle \mathbf{v}_l \rangle^l$, superimposed on the solid fraction, ϵ_s, isopleths at 10 s. The maximum solid fraction occurs along the lower third of the cooled wall, where the globulitic crystals have packed and the velocities are small. On the other hand, the solid fraction along the upper third of the cooled wall is small, indicating that the crystals are advected downwards. In fact, a considerable amount of solid is present near the lower (adiabatic) wall of the enclosure. Generally, the liquid flow consists of a counterclockwise rotating convection cell because of the cooling from the left wall and the fact that the rejected solute causes the liquid to be rich in copper. In other words, the thermal and solutal buoyancy forces at the left wall are augmenting each other. The temperature and liquid concentration pat-

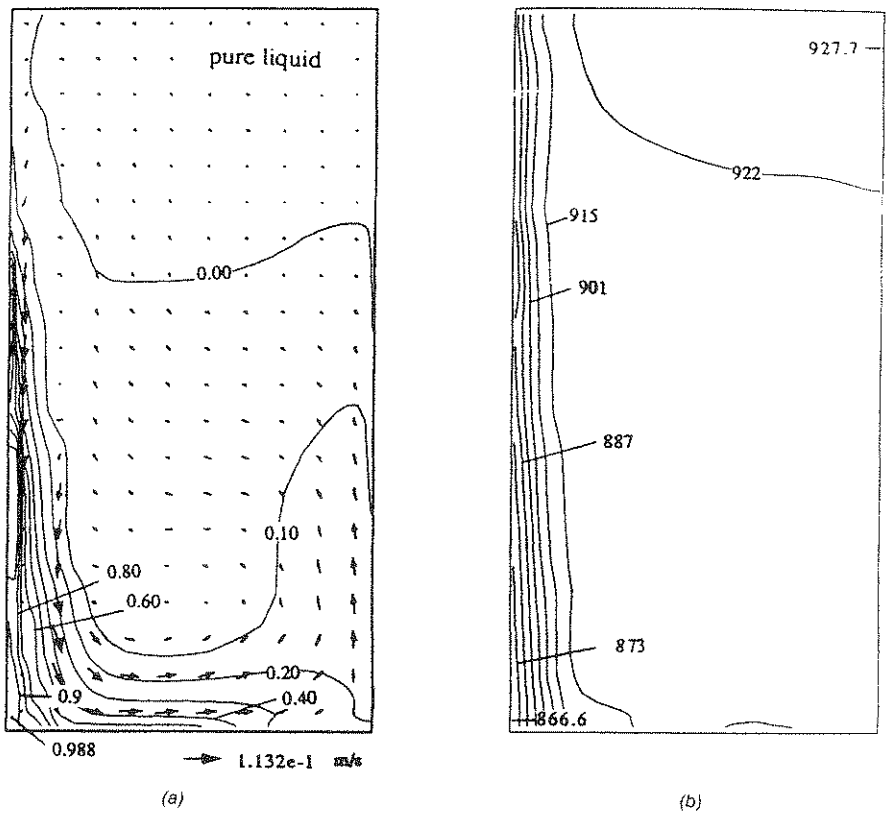

Figure 4. *Results at t = 10 s: (a) solid-liquid mixture velocity and solid volume fraction (equal increments, max = 0.988, min = 0.0); (b) isotherms (equal increments, max = 927.7 K, min = 866.6 K); (c) liquid species concentration (equal increments, max = 0.195, min = 0.029); (d) relative velocity between the liquid and solid phases.*

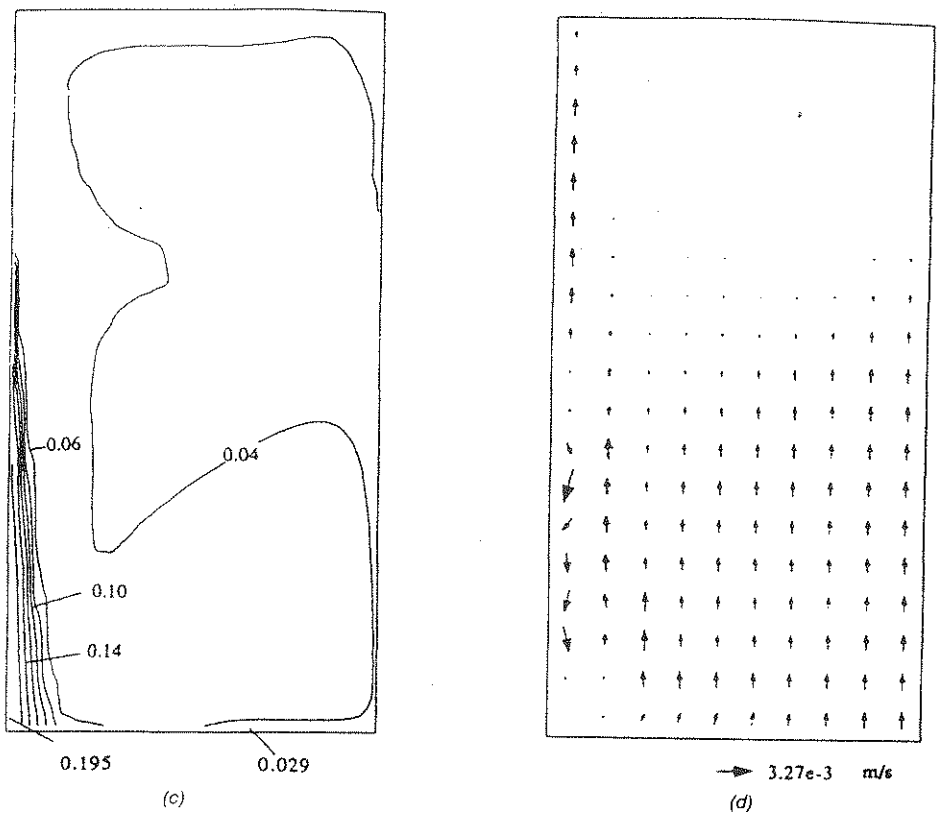

Figure 4 (continued). *Results at t = 10 s: (a) solid-liquid mixture velocity and solid volume fraction (equal increments, max = 0.988, min = 0.0); (b) isotherms (equal increments, max = 927.7 K, min = 866.6 K); (c) liquid species concentration (equal increments, max = 0.195, min = 0.029); (d) relative velocity between the liquid and solid phases.*

terns causing these buoyancy forces are shown in Figures 4(b) and 4(c), respectively. The liquid advects crystals to the right portion of the enclosure where the melt is still of the original composition and near the liquidus temperature. A pure liquid region ($\epsilon_s = 0$) only exists in the upper right portion of the enclosure. In order to illustrate the movement of the solid crystals relative to the liquid, the relative velocity vectors, $\langle \mathbf{v}_l \rangle^l - \langle \mathbf{v}_s \rangle^s$, are displayed in Figure 4(d). Note that the scale of the relative velocity vectors is almost two orders of magnitude smaller than the liquid velocity vectors of Figure 4(a). The relative velocities are mostly upward, implying that the downward (negative y-direction) component of the solid velocity is larger than that of the liquid. This can be explained by the fact that the solid has a larger density than the liquid, i.e., the crystals are sedimenting. The magnitude of the relative velocities decreases with decreasing solid fraction because the interfacial drag increases with decreasing crystal size. For a solid fraction greater than about 0.6, the crystals have packed and do not move so that the relative velocity vectors represent the liquid velocity only. This can be observed along the lower portion of the cooled wall, where the liquid percolates downward through the stationary bed of globulitic crystals. These velocities cannot be seen in Figure 4(a) due to the larger velocity scale used in this figure. In the lower left corner, the solid fraction is so large that all velocities vanish.

Results at 30 s are provided in Figures 5(a) to 5(f). As can be seen in Figure 5(a), solidification has progressed considerably. A pure solid region exists near the lower portion of the cooled wall, indicating that the temperature at these locations has fallen below the eutectic temperature [see also Figure 5(b)]. Virtually the entire enclosure is occupied by either stationary ($\epsilon_s > 0.637$) or moving ($\epsilon_s < 0.637$) globulitic crystals. An accumulation of sedimented crystals can be observed at the lower wall. The sedimentation process is also illustrated by the relative velocity vectors in Figure 5(d). However, a large amount of solid is advected with the liquid to the

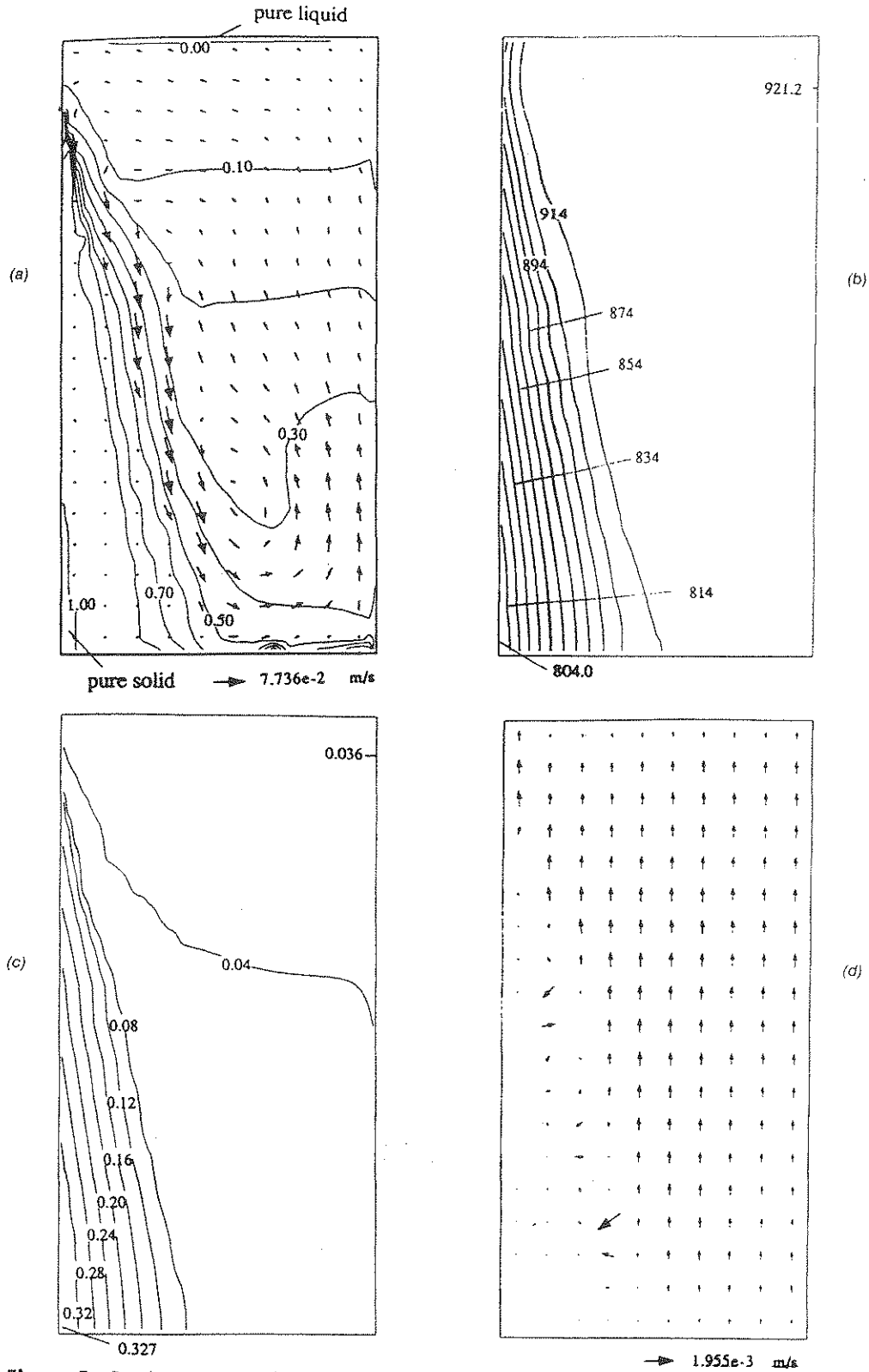

Figure 5. *Results at t = 30 s: (a) solid-liquid mixture velocity and solid volume fraction (equal increments, max = 1.0, min = 0.0); (b) isotherms (equal increments, max = 921.2 K, min = 804.0 K); (c) liquid species concentration (equal increments, max = 0.327, min = 0.036); (d) relative velocity between the liquid and solid phases; (e) solid phase change rate per unit volume (equal increments, max = 2367.3 kg/m^3-s, min = 300.8 kg/m^3-s); (f) mixture species concentration (equal increments, max = 0.056, min = 0.01).*

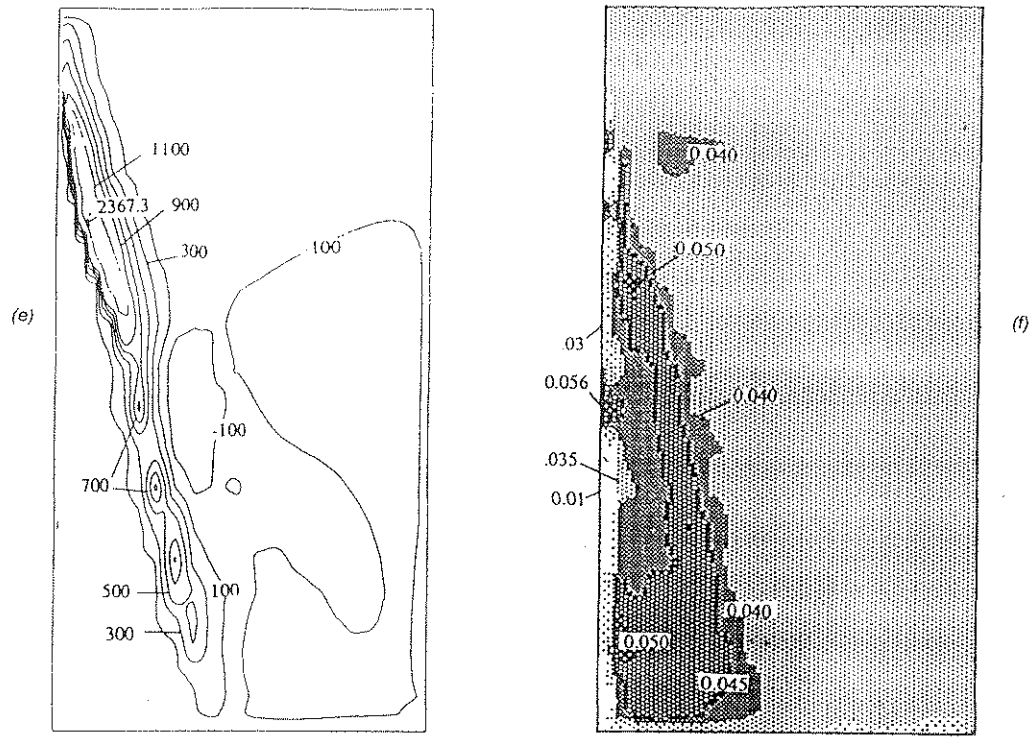

Figure 5 (continued). *Results at t = 30 s: (a) solid-liquid mixture velocity and solid volume fraction (equal increments, max = 1.0, min = 0.0); (b) isotherms (equal increments, max = 921.2 K, min = 804.0 K); (c) liquid species concentration (equal increments, max = 0.327, min = 0.036); (d) relative velocity between the liquid and solid phases; (e) solid phase change rate per unit volume (equal increments, max = 2367.3 kg/m³-s, min = 300.8 kg/m³-s); (f) mixture species concentration (equal increments, max = 0.056, min = 0.01).*

right and upper portions of the enclosure into regions of higher temperature. The fate of these crystals can be inferred from Figure 5(e), where the local phase change rate, Γ_s, is plotted. The entire right half of the enclosure is characterized by a negative Γ_s, which implies that remelting is taking place. Most of the solidification occurs along the edge of the stationary bed of globulitic crystals, indicating that the solutal undercooling is the largest in this region. The mixture concentration field, shown in Figure 5(f), illustrates the evolution of macrosegregation due to the relative motion between the liquid and solid phases. Deviations from the initial composition (C_{in} = 0.04) are limited to regions of higher solid fraction. Elsewhere, the relative velocities are too small to cause appreciable macrosegregation. A mixture concentration below the initial melt composition can be observed in the lower right portion of the enclosure and adjacent to the cooled wall. This may be explained by the sedimentation of solute poor crystals. It has been confirmed that the average mixture concentration for the entire enclosure remains at the initial value.

The liquid velocities and solid fractions at 60 s and 90 s are shown in Figures 6 and 7, respectively. Due to space limitations, other results are omitted. The overall transport phenomena are similar to those at 30 s, with the fully solidified region growing at the expense of the convecting two-phase region. Even at 60 s, the uppermost portion of the cooled wall is relatively free of the solid, which can be attributed to the downward flow of melt and crystals along the cooled wall. As expected, the upper right corner is the last region to solidify. Note that the magnitude of the velocity continually decreases.

Final macrosegregation and grain radius, R_f, patterns are displayed in Figures 8(a) and 8(b), respectively. Negative macrosegregation exists all along the cooled wall and in the lower right and upper left portions of the enclosure, except in the upper left corner, where the concentration is near the eutectic value. The large positive macrosegregation in the upper left corner

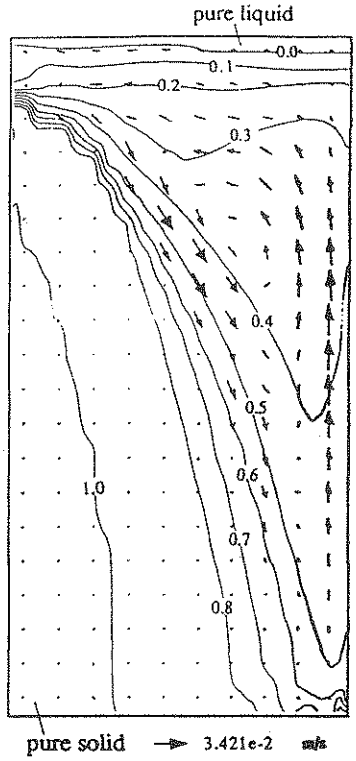

Figure 6. *Solid-liquid mixture velocity and solid volume fraction at t = 60 s (equal increments, max = 1.0, min = 0.0).*

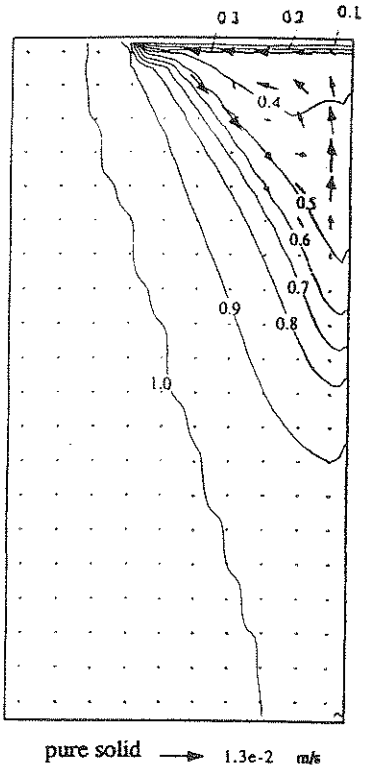

Figure 7. *Solid-liquid mixture velocity and solid volume fraction at t = 90 s (equal increments, max = 1.0, min = 0.013).*

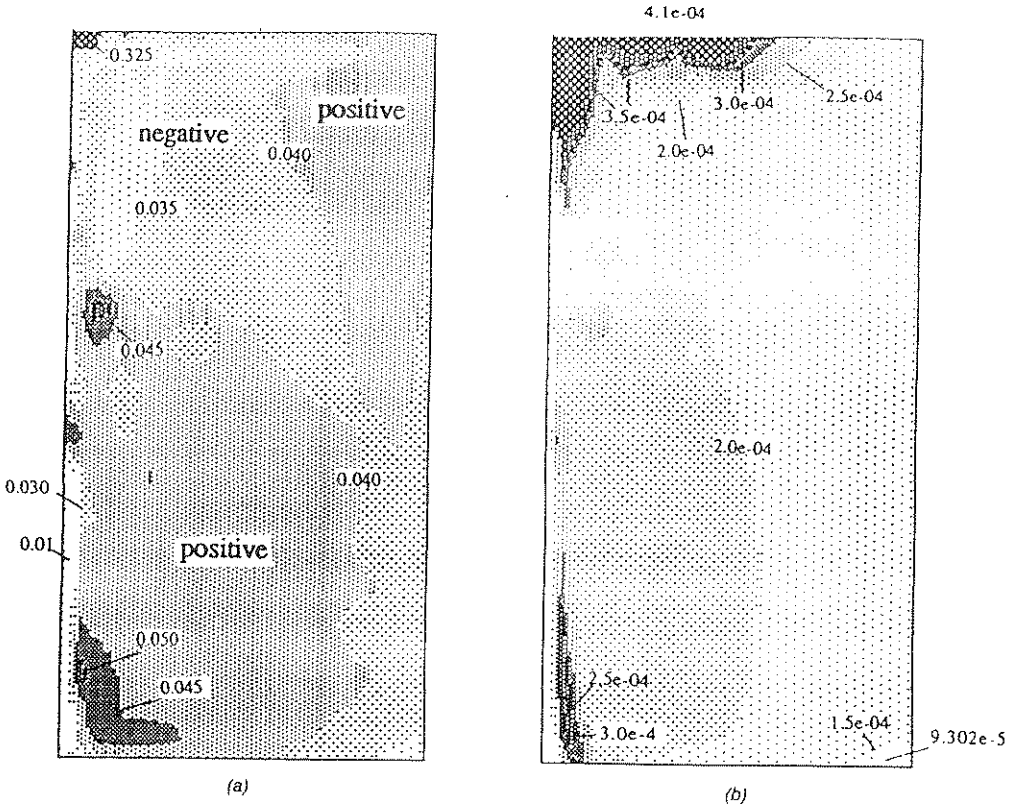

Figure 8. *Final results for the fully solidified enclosure (t = 117 s): (a) macrosegregation pattern (equal increments, max = 0.325, min = 8.77 × 10⁻³); (b) grain radius distribution (equal increments, max = 4.1 × 10⁻³ m, min = 9 × 10⁻⁵ m).*

is caused by the continual flow of the solute poor crystals out of this region (see also Figure 6) such that a stationary solid structure only forms when the temperature is already close to the eutectic value. Relatively little positive macrosegregation can be observed in the upper right portion of the enclosure. Another interesting outcome of the simulation is the final grain size distribution, as shown in Figure 8(b). Recall that the grain density, n, is obtained from the solution of Equation (2). Then, with the knowledge of the local solid fraction, the equivalent sphere radius, R_s, can be calculated, until solidification is complete (see Table 4). An examination of Equation (2) reveals that in the absence of solid motion ($\langle \mathbf{v}_s \rangle^s = 0$), the grain density would be uniformly equal to 10^{11} 1/m³, which corresponds to a final grain radius of 1.34×10^{-4} m. This is because the nucleation rate given by Equation (3) was taken as a constant (i.e., $K_2 = 0$, see Table 3). Consequently, all nonuniformities in the final grain size distribution can be directly attributed to solid motion. Although a constant nucleation rate is not realistic, it aids in clarifying the effects of solid motion in this exploratory simulation. It can be seen that a grain radius of approximately 100 μm only exists in the lower left and right corners. The grain radii in the middle portion of the enclosure are about twice as large, and even larger grains can be found in the upper left portion. The larger grain radii can be explained by the transport and remelting of grains. Initially, a large number of grains settled in the lower corners and continued to grow. However, grains advected to superheated regions of the enclosure remelted (see Figures 4 and 5), causing a reduction in the overall grain density, particularly in the upper portions at the castings.

CONCLUSIONS

A volume-averaged two-phase model was used to predict transport phenomena during glob-

ulitic solidification of a binary metal alloy. The model incorporates nucleation, thermal and solutal undercooling, and interfacial drag, together with heat transfer, solute redistribution, melt convection, and solid transport on the system scale. The results reveal the effect of thermosolutal convection, sedimentation, and remelting on the evolution of macrosegregation and the final grain size distribution.

Although an exploratory numerical simulation has been successfully performed, considerable additional research is required before the model can be applied to real metal castings. In this respect, the following items deserve special attention: (1) nucleation and the origin of globulitic grains in the presence of convection; (2) the interfacial drag, and heat and mass transfer coefficients (i.e., diffusion lengths), and (3) the macroscopic transport coefficients, particularly the effective solid and liquid viscosities. Specially designed experiments are needed to determine these coefficients for a solidifying system. In addition, more numerical simulations, for example without solid transport, should be performed to investigate the system dynamics in more detail. Work is also under way to extend the model to equiaxed dendritic growth (Wang and Beckermann, 1993).

ACKNOWLEDGEMENTS

The authors would like to acknowledge financial support from the National Science Foundation under grants CBT-8808888 and CTS-8957149 and by the ALCOA Technical Center. Computer facilities were made available by the University of Iowa WEEG Computing Center.

REFERENCES

Agarwal, P. K. and B. K. O'Neill. 1988. "Transport Phenomena in Multi-Particle System—I. Pressure Drop and Friction Factors: Unifying the Hydraulic-Radius and Submerged-Object Approaches," *Chem. Engng. Sci.*, 43(9):2487–2499.

Battle, T. P. and R. D. Pehlke. 1990. "Mathematical Modeling of Microsegregation in Binary Metallic Alloys," *Metall. Trans. B.*, 21B:357–375.

Ding, J. and D. Gidaspow. 1990. "A Bubbling Fluidization Model Using Kinetic Theory of Granular Flow," *AIChE Journal*, 36(4):523–538.

Feller, R. J. 1991. "Modeling the Equiaxed Solidification of Binary Alloys," M.S.M.E. thesis, The University of Iowa, Iowa City, IA 52242.

Feller, R. J. and C. Beckermann. 1993. "Modeling of the Globulitic Solidification of a Binary Metal Alloy," *International Communications in Heat & Mass Transfer*, 20:311–322.

Flemings, M. C. 1974. *Solidification Processing*. New York: McGraw-Hill.

Ganesan, S. and D. R. Poirier. 1987. "Densities of Aluminum-Rich Aluminum-Copper Alloys during Solidification," *Metall. Trans. A*, 18A:721–723.

Hatch, J. 1984. *Aluminum: Properties and Physical Metallurgy*. Metals Park, OH: American Society for Metals.

Incropera, F. P. and R. Viskanta. 1990. "Effects of Convection on the Solidification of Binary Mixtures," presented at *Oji International Seminar on Advanced Heat Transfer in Manufacturing and Processing of New Materials, Tomakomai, Hokkaido, Japan, October 28–31.*

Ludwig, J. C., H. Q. Qin and D. B. Spalding. 1989. *The PHOENICS Reference Manual*, CHAM TR/200.

Ni, J. 1991. "Development of a Two-Phase Model of Transport Phenomena during Equiaxed Solidification," Ph.D. thesis, The University of Iowa, Iowa City, IA, Dec. 9.

Ni, J. and C. Beckermann. 1990. "A Two-Phase Model for Mass, Momentum, Heat, and Species Transport during Solidification," *Transport Phenomena in Material Processing, Vol. 132*, M. Charmichi, M. K. Chyu, Y. Joshi and S. M. Walsh, eds., New York: ASME, HTD, pp. 45–56.

Ni, J. and C. Beckermann. 1991. "A Volume-Averaged Two-Phase Model for Transport Phenomena during Solidification," *Metall. Trans. B*, 22B:349–361.

Ni, J., R. J. Feller and C. Beckermann. 1990. "A Two-Phase Model of Transport Phenomena during Solidification," presented at the *Conference on Modeling of Casting, Welding and Advanced Solidification Processes, Engineering Foundation Conference, Davos, Switzerland, Sept. 16–21.*

Prakash, C. 1990a. "Two-Phase Model for Binary Solid-Liquid Phase Change, Part I: Governing Equations," *Numerical Heat Transfer, Part B*, 18:131–145.

Prakash, C. 1990b. "Two-Phase Model for Binary Solid-Liquid Phase Change, Part II: Some Illustrative Examples," *Numerical Heat Transfer, Part B*, 18:147–167.

Rappaz, M. 1989. "Modelling of Microstructure Formation in Solidification Processes," *Int. Materials Reviews*, 34:93–123.

Rowe, P. N. and K. T. Claxton. 1965. "Heat and Mass Transfer from a Single Sphere to Fluid Flowing through an Array," *Trans. Instn. Chem. Engrs.*, 43:T321–T331.

Stefanescu, D. M., G. Upadhya and D. Bandyopadhyay. 1990. "Heat Transfer-Solidification Kinetics Modeling of Solidification of Castings," *Metall. Trans. A*, 21A:997–1005.

Thevoz, Ph., J. L. Desbiolles and M. Rappaz. 1989. "Modeling of Equiaxed Microstructure Formation in Casting," *Metall. Trans. A*, 20A:311–322.

Wang, C. Y. and C. Beckermann. In press. "A Multiphase Model of Solute Diffusion in Dendritic Alloy Solidification," *Metall. Trans. A.*